JOURNAL OF COMPUTATIONAL PHYSICS **88**, 183–204 (1990)

Full-Wave Calculations in Flux Coordinates for Toroidal Geometry*

B. A. CARRERAS, V. E. LYNCH,[†] E. F. JAEGER,
D. B. BATCHELOR, AND J. S. TOLLIVER

Oak Ridge National Laboratory, Oak Ridge, Tennessee 37831-8071

Received July 11, 1988; revised June 12, 1989

A two-dimensional (2D) full-wave code, HYPERION, employing a poloidal and toroidal mode expansion and including the toroidal terms arising in the wave equation, has been developed. It is based on the existing modules developed for the MHD stability codes. The plasma response is described by the collisionally broadened cold-plasma conductivity tensor. The code retains the $E_{\parallel}$ component of the electric field, which allows the study of the low-density resion of the plasma. A detailed benchmarking of the HYPERION code has been done with the existing finite-difference full-wave code ORION.

1. INTRODUCTION

The modeling of excitation, propagation, and absorption of electromagnetic waves in the ion cyclotron range of frequencies (ICRF) has become a problem of considerable importance for the heating of large tokamaks in fusion research. Because of the large size of antenna structures and the free-space wavelength in this frequency range ($f \sim 30$–100 MHz) and because of the presence of wave resonances and cutoffs in the plasma, geometrical optics methods fail, and a full-wave solution is needed. A number of large codes have been developed to calculate ICRF wave heating in fusion devices [1–6]; they employ a variety of numerical methods and cover a wide range of detail of the physical models for plasma dispersion and absorption. For the most part, these codes have assumed one ignorable coordinate (either toroidal or helical), allowing a Fourier decomposition in the ignorable direction. The codes can then be classified according to whether the remaining two-dimensional (2D) problem is solved by finite-difference (or finite-element) methods [1, 3] or by a further Fourier decomposition in a nonignorable direction to yield a set of coupled equations for each Fourier mode [4–6]. In this paper, we describe

---

* Research sponsored by the Office of Fusion Energy, U.S. Department of Energy, under contract DE-AC05-84OR21400 with Martin Marietta Energy Systems, Inc. The U.S. Government's right to retain a nonexclusive royalty-free license in and to the copyright covering this paper, for governmental purposes, is acknowledged.

[†] Computing and Telecommunications Division, Martin Marietta Energy Systems, Inc.

0021-9991/90 $3.00

a new code HYPERION, based on a poloidal mode expansion, and make detailed comparisons with an existing 2D finite-difference code, ORION [1].

Smithe *et al.* [4] have developed a poloidal mode expansion code in which the geometry is fundamentally cylindrical, with the equilibrium magnetic field in the z direction and varying in the x direction as $B = B_0/(1 + x/R_0)$. Although only the fast wave is treated in this code, certain effects of the electrostatic Bernstein mode on the fast wave are retained by using the warm-plasma conductivity tensor expanded to second order in Larmor radius and inserting $k_\perp$ as obtained from the warm, uniform plasma dispersion relation into $\sigma(k_{\|}, k_\perp)$. Because of the large electron conductivity parallel to B, $E_{\|}$ is assumed to be negligible. This, of course, eliminates the cold-plasma slow wave. The coupled radial equations are solved by shooting methods.

Brambilla and Krücken [5] have developed a very general code based on a poloidal mode expansion that includes full toroidal equilibrium geometry, ion cyclotron damping through the presence of plasma dispersion functions at resonance, and transit time magnetic pumping. By including $E_{\|}$ as a perturbation, they have allowed for electron Landau damping. Also, by expanding the plasma current response to second order in Larmor radius, they obtain a fourth-order differential system that includes directly the coupling to the slow Bernstein mode. The radial equations are discretized using finite elements based on cubic Hermite basis functions. Because of the short wavelength of the Bernstein wave, a very dense mesh must be used. This severely limits the size and maximum density of tokamaks for which convergence can be obtained. So far, the code has been used only for devices with circular cross sections.

Gambier *et al.* have developed a code that contains physics similar to that in Brambilla and Krücken's code [5] but is based on a quite different variational formulation [6]. A quadratic functional is extremalized with respect to a set of linear finite-element basis functions. A time history integral is performed over unperturbed particle orbits; this permits treatment of the nonlocal effects due to the presence of a poloidal field. The codes of both Brambilla and Krücken [5] and Gambier *et al.* [6] require artificial damping of the Bernstein wave in order to limit the minimum wavelengths produced.

The HYPERION code described here is written in straight-field-line flux coordinates and retains the $E_{\|}$ component of the wave electric field. This allows the study of the low-density edge region of the plasma, which is a critical issue for coupling and impurity generation. A unique feature of HYPERION is the removal of resonant denominators through multiplication of $\Pi_j(\omega^2 - \Omega_j^2)$. In this way the poloidaly varying coefficients can be expressed directly as convolutions of the Fourier expansions of the equilibrium quantities, and no additional Fourier transforms are required. Experience with MHD computations has shown that this technique greatly increases speed and accuracy. One of the principal advantages of the poloidal mode expansion is that the $\mathbf{B} \cdot \nabla$ operator is algebraic rather than differential, which greatly facilitates the inclusion of kinetic and nonlocal effects when a poloidal field is present. This work is in progress. This advantage does not enter into the present work since, for the initial version of the code, we consider only the cold-plasma conductivity with an effective collisionality to broaden the cyclotron resonances. In this paper we concentrate on benchmarking HYPERION against a 2D finite-difference code, on convergence studies, and on the effects of toroidal geometry on heating results. In Section 2, we present the wave equations in our flux coordinate system. In Section 3, we describe the numerical approach taken. In Section 4, we make a detailed comparison of the HYPERION code with ORION and present the results of convergence studies. In Section 5, we investigate the importance of toroidicity on fast wave heating for inside and outside antenna positions by varying the aspect ratio.

2. EQUATIONS

To study the full-wave propagation in a tokamak geometry for the appropriate frequency range, the starting point is Maxwell's equations combined with a model for the plasma response, which for this paper is restricted to the cold-plasma approximation. In this paper, only the linear wave propagation problem is considered. Under this assumption, the time dependence of the oscillating fields is given by $e^{i\omega t}$, and the equations are

$$\begin{aligned} \nabla \times \mathbf{E} &= i\omega \mathbf{B}, \\ \nabla \times \mathbf{B} &= \mu_0 \mathbf{J}_{\text{ext}} - i\omega \varepsilon_0 \mu_0 K \cdot \mathbf{E}. \end{aligned} \tag{1}$$

Here $\mathbf{J}_{\text{ext}}$ is the current density external to the plasma, which in practice is the current density at the antenna, and K is the dielectric tensor in the cold-plasma approximation. In the reference frame in which the equilibrium magnetic field $\mathbf{B}_{\text{eq}}$ is in the z-direction, the tensor K has the form

$$\begin{pmatrix} K_\perp & iK_x & 0 \\ -iK_x & K_\perp & 0 \\ 0 & 0 & K_\| \end{pmatrix}, \tag{2}$$

with

$$K_\perp = 1 - \sum_j \frac{\omega_{pj}^2}{\omega^2 - \Omega_j^2}, \qquad K_x = \sum_j \frac{\Omega_j}{\omega} \frac{\omega_{pj}^2}{\omega^2 - \Omega_j^2}, \qquad K_\| = 1 - \sum_j \frac{\omega_{pj}^2}{\omega^2}, \tag{3}$$

where $\omega_{pj}^2 = (q_j^2 n_j)/(\varepsilon_0 m_j)$ is the plasma frequency for the species j, ω is the externally excited frequency, and $\Omega_j = (q_j |\mathbf{B}_{\text{eq}}|)/m_j$ is the cyclotron frequency for species j. Here m_j is the mass, q_j is the charge, and n_j is the density of species j. The notation and conventions are the same as those used by Jaeger *et al.* [1]; more details can be found in that work.

As discussed in Section 1, it is desirable in solving the wave propagation equation in toroidal geometry and the ICRF to have a good representation for $k_{\|}$. To do so, we need an adequate numerical representation of the operator $\mathbf{B}_{\text{eq}} \cdot \nabla$. It is, then, appropriate to use a coordinate system (ρ, θ, ζ) in which the magnetic field lines are straight. In particular, we choose ρ to be a flux variable, normalized such that $\rho = 0$ is at the magnetic axis and $\rho = 1$ at the plasma edge. The third coordinate, ζ, is the usual toroidal angle, and the poloidal angle θ is chosen such that

$$\mathbf{B}_{\text{eq}} \cdot \nabla \propto \frac{\partial}{\partial \theta} - q(\rho) \frac{\partial}{\partial \zeta}, \tag{4}$$

where $q(\rho)$ is the safety factor. This condition implies that the Jacobian J of this coordinate system is given by

$$J = R^2 l, \tag{5}$$

where $R = R(\rho, \theta)$ is the radial coordinate in the usual toroidal reference system, that is, the distance to the axis of the torus, and

$$l = \frac{1}{4\pi^2} \int_V \frac{d\tau}{R^2}, \tag{6}$$

where the integral is extended to the whole plasma volume. From Eq. (6), it is possible to define an average plasma radius consistent with the metric by setting $a = (2R_0 l)^{1/2}$. This coordinate system has been extensively used in MHD stability calculations [7]. The price one pays for the advantages of this coordinate system is the nonorthogonality of the ρ and θ directions, which makes some of the terms in these equations more cumbersome. The equilibrium magnetic field in this coordinate system can be written as

$$\mathbf{B}_{\text{eq}} = \nabla\zeta \times \nabla\psi - F(\psi) \nabla\zeta, \tag{7}$$

where $F(\psi)$ is the toroidal magnetic field component times R, and ψ is the poloidal flux function, which in terms of the q profile is given by

$$\psi(\rho) = -\int_\rho^1 \rho \, d\rho \frac{F(\rho)}{q(\rho)}. \tag{8}$$

The ρ coordinate is now defined in such a way that the toroidal flux Φ is

$$\Phi = \frac{a^2}{R_0} \int_0^\rho F(\rho) \rho \, d\rho. \tag{9}$$

In the large-aspect-ratio limit, Eq. (9) becomes $\Phi = a^2 B_0 \rho^2 / 2$, where B_0 is the magnetic field at the center of the toroidal field coils. Therefore, ρ can be interpreted as a generalized minor radius, normalized to its value at the plasma edge.

Equation (1) is a linear system of partial differential equations for the oscillating electric, **E**, and magnetic, **B**, fields. A consequence of the axisymmetry of the equilibrium fields is that the toroidal wave number n is a good quantum number. Therefore, the oscillating fields can be Fourier expanded in the toroidal angle ζ. For each field component, A, we can write

$$A(\rho, \theta, \zeta) = \sum_n A_n(\rho, \theta) e^{in\zeta} \tag{10}$$

and, in this way, reduce the system of partial differential equations (1) in ρ, θ, ζ to a set of coupled partial differential equations in ρ, θ for each value of n. The set of equations for a given n value can be written as

$$n\varepsilon B_\rho = \omega R^2(g^{\theta\rho} B_\rho + g^{\theta\theta} B_\theta) - i\frac{\partial E_\zeta}{\partial \rho}, \tag{11}$$

$$n\varepsilon E_\theta = -\omega R^2(g^{\rho\rho} B_\rho + g^{\rho\theta} B_\theta) - i\frac{1}{\rho}\frac{\partial E_\zeta}{\partial \theta}, \tag{12}$$

$$n\varepsilon B_\rho = -\omega(\alpha^{\theta\rho} E_\rho + \alpha^{\theta\theta} E_\theta + \alpha^{\theta\zeta}\varepsilon E_\zeta) - iJ^\theta R^2 - i\frac{\partial B_\zeta}{\partial \rho}, \tag{13}$$

$$n\varepsilon B_\theta = \omega(\alpha^{\rho\rho} E_\rho + \alpha^{\rho\theta} E_\theta + \alpha^{\rho\zeta}\varepsilon E_\zeta) + iJ^\rho R^2 - i\frac{1}{\rho}\frac{\partial B_\zeta}{\partial \theta}, \tag{14}$$

$$0 = \frac{1}{\rho}\frac{\partial(\rho B_\theta)}{\partial \rho} - \frac{1}{\rho}\frac{\partial B_\rho}{\partial \theta} + i\omega(\varepsilon\alpha^{\zeta\rho} E_\rho + \varepsilon\alpha^{\zeta\theta} E_\theta + \alpha^{\zeta\zeta} E_\zeta) - J^\zeta R^2, \tag{15}$$

$$0 = \frac{1}{\rho}\frac{\partial E_\rho}{\partial \theta} - \frac{1}{\rho}\frac{\partial \rho E_\theta}{\partial \rho} + i\omega B_\zeta. \tag{16}$$

Here, g^{ij} is the metric tensor, and for simplicity the subindex n has been dropped from the components of the oscillating fields. If T is the matrix associated with the coordinate transformation, the dielectric tensor in this coordinate system can be calculated by $(\alpha^{ij}) = TKT^{-1}$. This leads to the following form for the dielectric tensor,

$$\alpha^{\rho\rho} = R^2 g^{\rho\rho} K_\perp,$$

$$\alpha^{\rho\theta} = R^2 g^{\rho\theta} K_\perp + iK_x \frac{F}{R_0 B},$$

$$\alpha^{\rho\zeta} = g^{\rho\rho} \frac{\rho}{q} iK_x \frac{F}{R_0 B},$$

$$\alpha^{\theta\rho} = R^2 g^{\theta\rho} K_\perp - iK_x \frac{F}{R_0 B},$$

$$\alpha^{\theta\theta} = R^2 g^{\theta\theta} K_\perp + (K_\perp - K_\parallel)\left(\frac{F\rho\varepsilon}{RBq}\right)^2$$

$$\alpha^{\theta\zeta}=\frac{\rho}{q}\left[ig^{\rho\theta}K_x\frac{F}{R_0B}+(K_\perp-K_{||})\left(\frac{F}{RB}\right)^2\right],$$

$$\alpha^{\zeta\rho}=-g^{\rho\rho}\frac{\rho}{q}iK_x\frac{F}{R_0B},$$

$$\alpha^{\zeta\theta}=-\frac{\rho}{q}\left[ig^{\rho\theta}K_x\frac{F}{R_0B}-(K_\perp-K_{||})\left(\frac{F}{RB}\right)^2\right],$$

$$\alpha^{\zeta\zeta}=K_\perp-(K_\perp-K_{||})\left(\frac{F}{RB}\right)^2 \tag{17}$$

where $B=|\mathbf{B}_{\text{eq}}|$. These equations are written in dimensionless form. The lengths are normalized to the generalized minor radius a, R to the major radius R_0, the times to $\tau_0=a/c$, the magnetic field to the value of the toroidal field at the magnetic axis B_0, and the electric field to $E_0=aB_0/\tau_0$. The inverse aspect ratio is $\varepsilon=a/R_0$.

A problem with Eqs. (11)–(16) is the singular behavior of the solutions at the two-ion hybrid layer. This singular behavior is a consequence of the cold-plasma approximation, which is replaced by conversion to Bernstein modes when finite temperature effects are included. A standard way of removing the singularity in the cold-plasma approximation is to introduce an effective collisionality ν. This can be done heuristically by replacing the particle mass m_j by the complex number $m_j(1+i\nu/\omega)$. The consequences of this prescription have been discussed in detail by Jaeger *et al.* [1] and by Villard *et al.* [3]. The effect of ν on the numerical results and the range of ν values possible with the present code are discussed in Section 4.

For the typical plasma densities in the tokamak interior, the $K_{||}$ component of the dielectric tensor is of the order of m_i/m_e times the other matrix elements. This causes the parallel component of the electric field,

$$E_{||}=\frac{FR_0}{R^2B}\left(\frac{\rho\varepsilon}{q}E_\theta-E_\zeta\right), \tag{18}$$

to be smaller than the other electric field components by the inverse mass ratio. As a consequence, it has been assumed to be zero in most codes analogous to the one presented here. However, for low plasma densities, typical of plasma edge, the lower hybrid resonance can be in the plasma, and the role of the $E_{||}$ component becomes important. For this reason, the possibility of a nonzero $E_{||}$ has been retained in the present calculations. To avoid numerical pollution due to the disparity of scales in the parallel direction, Eq. (13) can be written as

$$n\varepsilon B_\rho=\left[\frac{1}{\rho}\frac{\partial(\rho B_\theta)}{\partial\rho}-\frac{1}{\rho}\frac{\partial B_\rho}{\partial\theta}\right]-\omega(\bar{\alpha}^\rho E_\rho+\bar{\alpha}^\theta E_\theta+\varepsilon\bar{\alpha}^\zeta E_\zeta)$$
$$-i\left(J^\theta_{\text{ext}}+\frac{\rho\varepsilon}{q}J^\zeta_{\text{ext}}\right)R^2-i\frac{\partial B_\zeta}{\partial\rho}, \tag{19}$$

where

$$\bar{\alpha}^{\rho} = R^2 g^{\theta\rho} K_{\perp} - i \frac{FK_x}{R_0 B}\left(1 + \frac{\rho^2\varepsilon^2}{q^2} g^{\rho\rho}\right), \tag{20}$$

$$\bar{\alpha}^{\theta} = R^2 g^{\theta\theta} K_{\perp} - i \frac{FK_x}{R_0 B} \frac{\rho^2\varepsilon^2}{q^2} g^{\rho\theta}, \tag{21}$$

$$\bar{\alpha}^{\zeta} = \frac{\rho}{q} K_{\perp} + i \frac{FK_x}{R_0 B} \frac{\rho}{q} g^{\rho\theta}. \tag{22}$$

If Eqs. (11), (12), (14)–(16), and (19) are used in solving the wave propagation problem, the only equation containing $K_{\parallel}$ is Eq. (15). When the $E_{\parallel} = 0$ approximation is desired, Eq. (15) is replaced by

$$\frac{\rho\varepsilon}{q} E_{\theta} = E_{\zeta}. \tag{23}$$

Equations (11), (12), (14), (16), and (19), with either Eq. (15) or Eq. (23), are the equations solved by the numerical scheme described in Section 3.

3. Numerical Approach and Code Implementation

Equations (11), (12), (14), (16), and (19), with either Eq. (15) or Eqs. (23), have been implemented in a 2D code called HYPERION. This code employs a poloidal mode expansion and finite differences in the generalized radial coordinate ρ. It is based on existing modules developed for the MHD stability codes [8] and uses as input the tokamak equilibria calculated with the RSTEQ code [9].

The first step in the discretization of these equations is the expanson of the oscillating field components in the poloidal angle variable θ. For a general component A, the expansion in Fourier harmonics is

$$A_n(\rho, \theta) = \sum_{m=0}^{M} A_{n,m}(\rho) \cos(m\theta) + \sum_{m=1}^{M} A_{n,-m}(\rho) \sin(m\theta). \tag{24}$$

Here, the amplitudes $A_{n,m}$ are complex numbers, and the maximum number of poloidal mode components for the oscillating fields included in the calculation is M.

The input equilibrium parameters are the real space coordinates of the flux surfaces, $R(\rho, \theta)$ and $Z(\rho, \theta)$, and the metric elements $g^{ij}(\rho, \theta)$. They are given as a Fourier series expansion,

$$R(\rho, \theta) = \sum_{m=0}^{\bar{M}} R_m(\rho) \cos(m\theta), \tag{25}$$

$$Z(\rho, \theta) = \sum_{m=1}^{\bar{M}} Z_m(\rho) \sin(m\theta), \tag{26}$$

$$g^{ij}(\rho, \theta) = \sum_{m=1}^{\bar{M}} g^{ij}_m(\rho) \sin(m\theta), \qquad i \neq j, \tag{27}$$

$$g^{ij}(\rho, \theta) = \sum_{m=0}^{\bar{M}} g^{ij}_m(\rho) \cos(m\theta), \qquad i = j, \tag{28}$$

where $\bar{M}$ is the maximum poloidal mode number included in the representation of the equilibrium fields; in general, it is different from M. All Fourier coefficients in Eqs. (25)–(28) are real, and the symmetries of the expansion reflect the assumed up–down symmetry of the equilibrium.

The elements of the dielectric tensor have an equilibrium magnetic field dependence in the denominators through the cyclotron frequencies, which can lead to singularities for these elements, although they do not correspond to singularities of the equations. Direct treatment of these singularities would require the calculation of these elements in real space, plus a very accurate Fourier transform back to Fourier space. The accuracy required and the number of operations involved could be a serious drawback for the Fourier expansion method. An alternative solution is to remove these denominators of the α^{ij} terms by multiplying Eqs. (14), (15), and (19) by the function

$$\Gamma = \prod_j \left\{ \left[(\omega^2 - \nu^2) \left(\frac{R}{R_0} \right)^2 - \Omega_{0j}^2 f(\rho, \theta) \right]^2 + 4\omega^2 \nu^2 \left(\frac{R}{R_0} \right)^4 \right\}; \tag{29}$$

here, Ω_0 is just Ω_j with B changed to B_0. Therefore, Ω_{0j} is constant. The function f is

$$f(\rho, \theta) = \frac{F}{R_0 B_0} \left(1 + \frac{\varepsilon^2 \rho^2}{q^2} g^{\rho\rho} \right) \equiv \left(\frac{RB}{R_0 B_0} \right)^2, \tag{30}$$

which an be expressed directly as a Fourier series in terms of the equilibrium expansion, Eq. (28). By multiplying the α^{ij} by Γ, all the singular denominators are removed. The αs become polynomials on R. Therefore, the α^{ij} can be directly expressed in terms of convolutions of the equilibrium parameters, and no Fourier transforms are required. This reduces the number of operations to be performed and increases the efficiency of the code.

The next step in the discretizaton of the equations is to set up a finite-difference scheme for the generalized radial variable ρ. A two-grid method is used, with the fields E_ρ, B_θ, and B_ζ defined on the half-grid points and the fields B_ρ, E_θ, and E_ζ on the integer grid points. In this scheme, Eqs. (12), (15), and (19) are solved on the integer grid points, while Eqs. (11), (14), and (16) are solved on the half-integer grid points. For most of the terms in these equations, there is an exact correspondence between variables and equations within this scheme. However, for a few terms a linear interpolation from the nearest-neighbor grod points is required.

Boundary values are needed only for the E_θ and E_ρ components, since these are the only components to appear in radial derivatives at integer grid points. A conducting wall boundary condition has been used,

$$(E_\theta)_{mn}|_{\rho=1} = (E_\zeta)_{mn}|_{\rho=1} = 0. \tag{31}$$

The regularity of the solution at the magnetic axis is imposed by requiring the ρ dependence

$$(E_\theta)_{mn} \approx \rho^{||m|-1|}, \tag{32}$$

$$(E_\zeta)_{mn} \approx \rho^{|m|}. \tag{33}$$

Given these boundary conditions, the discretized system of equations for each value of n can be solved by a block-tridiagonal matrix inversion. The matrix has $M_j - 1$ blocks on each diagonal, where M_j is the sum of the radial grid points on both the integer and half-integer radial grids. The odd-numbered blocks contain the equations defined on the half-integer grid, and the even-numbered blocks contain the integer grid equations.

Since each matrix is solved only once for each n, the speed of the matrix setup is more important than the speed of the solver. The software packages DECBT/SOLBT [10] and MA32 [11] have both been used for this matrix. DECBT/SOLBT solves a block-tridiagonal matrix that will fit in the memory of the computer. MA32 solves a sparse matrix using disk storage. The matrix setup for HYPERION enters the equation term by term, vectorized over the radial dimension of each term. Since MA32 writes the matrix to disk row by row, this vectorization cannot be used and the matrix setup is much slower. Both packages give the same solution, but the DECBT/SOLBT version runs much faster with the present matrix setup. Because the memory required is large and dominated by the size of the matrix, which is $3(M_j - 1)[N(2M+1)/2]^2$, where N is the number of equations, the National Magnetic Fusion Energy Computing Center Cray-2 must be used for this problem.

The density profile, $n(\rho)$, is a flux function, and for the calculations presented here, the profile parameterization is

$$\begin{aligned} n(\rho) &= (1 - n_{\text{edge}})\left[1 - \left(\frac{\rho}{\rho_p}\right)^2\right]^k + n_{\text{edge}}, && \rho \leqslant \rho_p \\ n(\rho) &= n_{\text{edge}}, && \rho_p \leqslant \rho \leqslant 1. \end{aligned} \tag{34}$$

The parameter ρ_p represents the plasma radius, outside of which a region of constant low density, n_{edge}, has been assumed. By including a non-zero edge density, nonphysical coaxial modes are eliminated. For the calculations presented here, n_{edge} is chosen sufficiently high as to also eliminate the lower-hybrid resonance. The exponent k allows one to change the density gradient in the plasma.

The antenna is located just inside the low-density region. The current density in the antenna is taken in the poloidal direction, and a parameterization similar to the one given by Jaeger *et al.* [1] has been used yielding a Gaussian current density profile centered at $\theta = 0$. The current density is

$$\mathbf{J}_{\text{ext}} = J^{\theta}_{\text{ext}} \nabla\theta, \tag{35}$$

where

$$J^{\theta}_{\text{ext}} = \frac{\mu_0 I_0}{aB_0} \delta(\rho - \rho_a) \frac{1}{D} \left[1 + 2 \sum_m \exp\left(-\frac{L_p^2 m^2}{4} \right) \cos m\theta \right] \sum \exp\left(-\frac{L_T^2 n^2}{4} \right) e^{in\zeta} . \tag{36}$$

with

$$D = \int_0^{2\pi} R^2 \left[1 + 2 \sum_m \exp\left(-\frac{L_p^2 m^2}{4} \right) \cos m\theta \right] d\theta. \tag{37}$$

Here L_p and L_T are the poloidal and toroidal lengths of the antenna, and I_0 is the total current in the antenna. For a given poloidal length of the antenna in real space, l_p, the poloidal length that appears in Eq. (36) is obtained from the equation

$$l_p = \frac{1}{R_0} \int_0^{L_p} \sqrt{R^2 g^{\rho\rho}}\, d\theta, \tag{38}$$

where the integral is taken over the flux surface $\rho = \rho_a$. In cylindrical geometry, $l_p = L_p$.

The main code diagnostics are 2D and three-dimensional (3D) plots of the $E_{\|}$ component; the right and left polarized electric field components, which in the straight-field-line coordinate system are given by

$$E_{\pm} = \frac{1}{\sqrt{g^{\rho\rho}}} \left[g^{\rho\rho} E_\rho + \left(g^{\rho\theta} \mp i \frac{FR_0}{R^2 B} \right) E_\theta \mp \frac{FR_0}{R^2 B} \frac{\varepsilon\rho g^{\rho\rho}}{q} E_\zeta \right]; \tag{39}$$

and the local energy deposition rate $\dot{W}$,

$$\begin{aligned} \dot{W}(\rho, \theta, n) = \frac{\omega}{2} \Big[& |E_{\|}|^2 \operatorname{Im} K_{\|} + \frac{1}{2} |E_+|^2 (\operatorname{Im} K_\perp - \operatorname{Im} K_x) \\ & + \frac{1}{2} |E_-|^2 (\operatorname{Im} K_\perp + \operatorname{Im} K_x) \Big], \end{aligned} \tag{40}$$

where $\dot{W}$ has been normalized to $(B_0)^2/(\mu_0\tau_0)$. The integration of $\dot{W}$ over the plasma volume leads to an energy conservation condition,

$$\tfrac{1}{2}\iint \rho\, d\rho\, d\theta\, R^2(\mathbf{E}\cdot\mathbf{J}^*_{\text{ext}}+\mathbf{E}^*\cdot\mathbf{J}_{\text{ext}})=\iint \rho\, d\rho\, d\theta\, \dot{W}(\rho,\theta,n), \tag{41}$$

which is a useful condition for checking the numerical convergence of the solution. Defining the power in the antenna by unit length as

$$P_n=\tfrac{1}{2}\iint \rho\, d\rho\, d\theta\, R^2\mathbf{E}\cdot\mathbf{J}^*_{\text{ext}}. \tag{42}$$

The total power absorbed by the plasma is obtained by adding the real part of P_n over the n spectrum and in a dimensional form is

$$P=2\pi R_0\frac{a^2B_0^2}{\mu_0\tau_0}\sum_n \operatorname{Re} P_n. \tag{43}$$

Dividing the power by $(I_0)^2/2$, one obtains the plasma loading resistance

$$\Re=\frac{2P}{I_0^2}=\frac{4\pi R_0a^2B_0^2}{\mu_0\tau_0I_0^2}\sum_n \operatorname{Re} P_n; \tag{44}$$

analogously, the antenna reactance is given by

$$\Im=\frac{4\pi R_0a^2B_0^2}{\mu_0\tau_0I_0^2}\sum_n \operatorname{Im} P_n. \tag{45}$$

4. Numerical Tests and Convergence Studies

To benchmark the HYPERION code, detailed comparisons were made with the ORION code [1], a 2D, finite-difference, full-wave code for ICRF fields in cylindrical geometry. The ORION code solves the equations in Cartesian coordinates and uses finite differences in the x and y directions. Details of the ORION code are given by Jaeger *et al.* [1].

The cylindrical geometry limit of the HYPERION code is set up by taking $R=R_0$, $g^{ij}=\delta_{ij}$, and $B=B_0/[1+\varepsilon\rho\cos(\theta)]$. Here, δ_{ij} is the Kronecker delta. The input equilibrium is analytically specified by giving a q and a density profile. Comparisons of the two codes have been done for several tokamak parameters. In particular, the effects of changing the aspect ratio and the position of the resonance surfaces have been studied in detail. The comparisons are illustrated with a case for the parameters of the tokamak fusion test reacter (TFTR), similar to a case studied by Smithe *et al.* [4]. The main parameters are

$$\begin{aligned} B_0 &= 4T \\ n(0) &= 3.3 \times 10^{13}\ \mathrm{cm}^{-3} \\ R_0 &= 3\ \mathrm{m} \\ a_{\mathrm{wall}} &= 1\ \mathrm{m} \\ a_{\mathrm{plasma}} &= 0.99\ \mathrm{m} \\ a_{\mathrm{antenna}} &= 0.95\ \mathrm{m} \\ \eta &= \frac{n(H)}{n(D)} = 0.05 \\ \frac{\nu}{\omega} &= 0.01 \\ f &= 55\ \mathrm{MHz}. \end{aligned}$$

The antenna is assumed to be a half-loop antenna with a poloidal width of $\pi/2$ and a toroidal length of 10 cm, and the plasma cross section is circular.

For these parameters, 3D plots of $|E_+|$ and $|E_-|$ are shown in Fig. 1 for the $n=7$ and in Fig. 2 for the $n=22$ toroidal components. These results show that the wave propagates from the antenna, located at the low-field side, toward the two-ion hybrid layer, where it is strongly absorbed. There is some level of transmission across the resonant layer, but it is rather small. Both codes reproduce all the features of the propagation and absorption, with good agreement between them, including the numerical magnitudes of the fields. The predictions of flux-surface-average power deposition (Fig. 3) are also very close.

Aspect ratio and plasma cross-section shaping are important geometrical parameters with a significant effect on the wave pattern. When the aspect ratio of the configuration and the frequency ω are changed so that the minority cyclotron resonance remains at a fixed minor radius, the spatial structure of the oscillating fields is substantially modified. For an $m=0$ antenna and the TFTR parameters given above, the $\dot{W}$ contours for aspect ratios of 3 and 12 are shown in Fig. 4. Both codes reproduce the main features of the local energy deposition rate, and the agreement remains very good. When the effect of the plasma cross-section shaping is included, the comparison of the results from the two codes is not so [illegible] HYPERION code, is not retained in the ORION code. Nevertheless, the qualitative agreement is good (Fig. 5).

In studying the numerical convergence of the solutions, there are three main parameters to consider: (1) the radial grid spacing $\Delta\rho$, (2) the maximum number of poloidal modes M, and (3) the effective collisionality parameter ν/ω. These parameters are strongly correlated, and to obtain a converged solution, the three must be properly adjusted. However, for clarity they are discussed here sequentially.

Let us consider only the ν/ω parameter. In this context, ν serves to resolve the singularities introduced by either the cyclotron resonance or hybrid resonances, rather than to model actual collisions. The value of ν/ω is chosen to broaden the resonance sufficiently that it can be resolved with finite grid spacing. Despite the ad hoc nature of this approach, a considerable body of experience shows that the energy absorption and large-scale field structure are determined by the asymptotic form of the dispersion and do not depend sensitively on the details of the singularity itself. In one-dimensional calculations [13], where direct comparison with full warm-plasma theory is possible, even the $k_{\|}$ dependence of the wave trans-

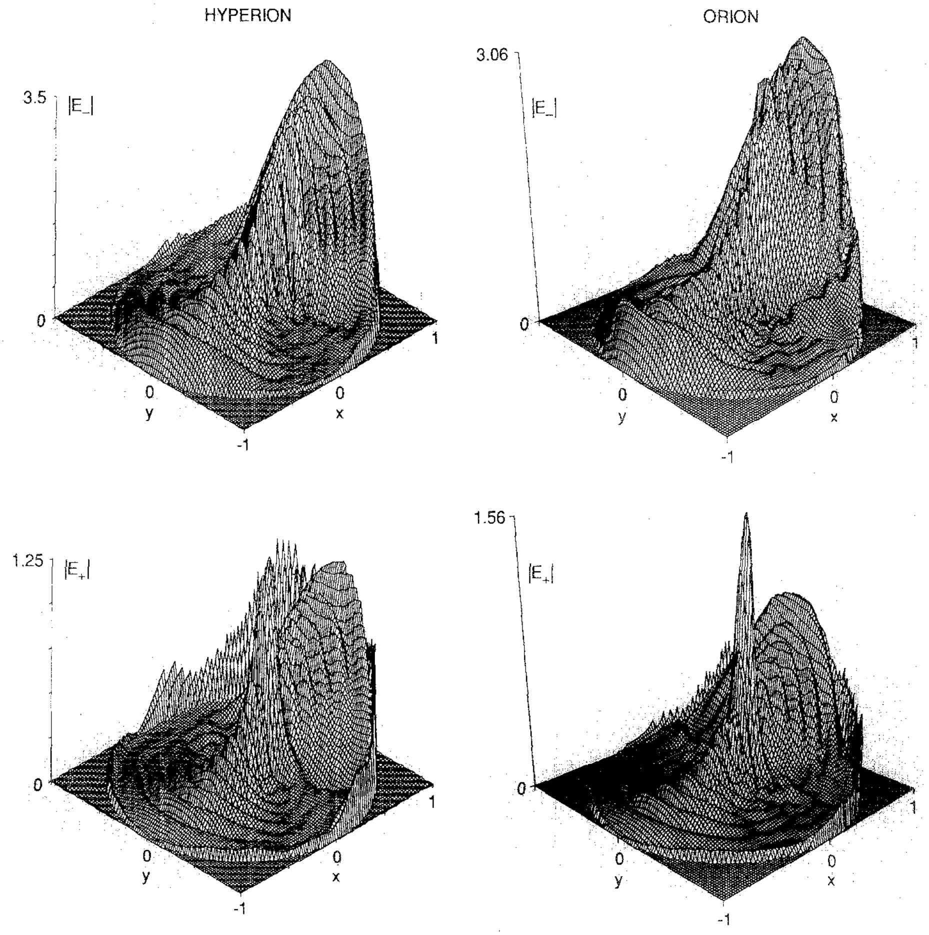

FIG. 1. 3D plots of $|E_+|$ and $|E_-|$ amplitudes in V/m for the $n=7$ toroidal component. The parameters are those for TFTR given in the text.

mission and reflection coefficients is reproduced by the collisional model. Of course, the partitioning of power between cyclotron damping and mode conversion is not obtained. As discussed by Villard *et al.* [3], for wave frequencies that are not near cavity modes, the dependence of the loading resistance on ν/ω is weak. As an example, the dependence of the loading resistance on ν/ω is plotted in Fig. 6 for the case of Fig. 1. Indeed, as ν/ω changes by a factor of 10, the resistance changes only be a factor of about 2. For $\nu/\omega > 2 \times 10^{-2}$, the resonance width is unrealistically broad, and the wave is too strongly damped. For $\nu/\omega < 10^{-3}$, the radial and poloidal resolution required to obtain a converged solution is too high for the present code to be used effectively. Therefore, most of the calculations have been done for the range $5 \times 10^{-3} < \nu/\omega < 10^{-2}$. Hereafter, it is assumed that ν/ω is in this parameter range.

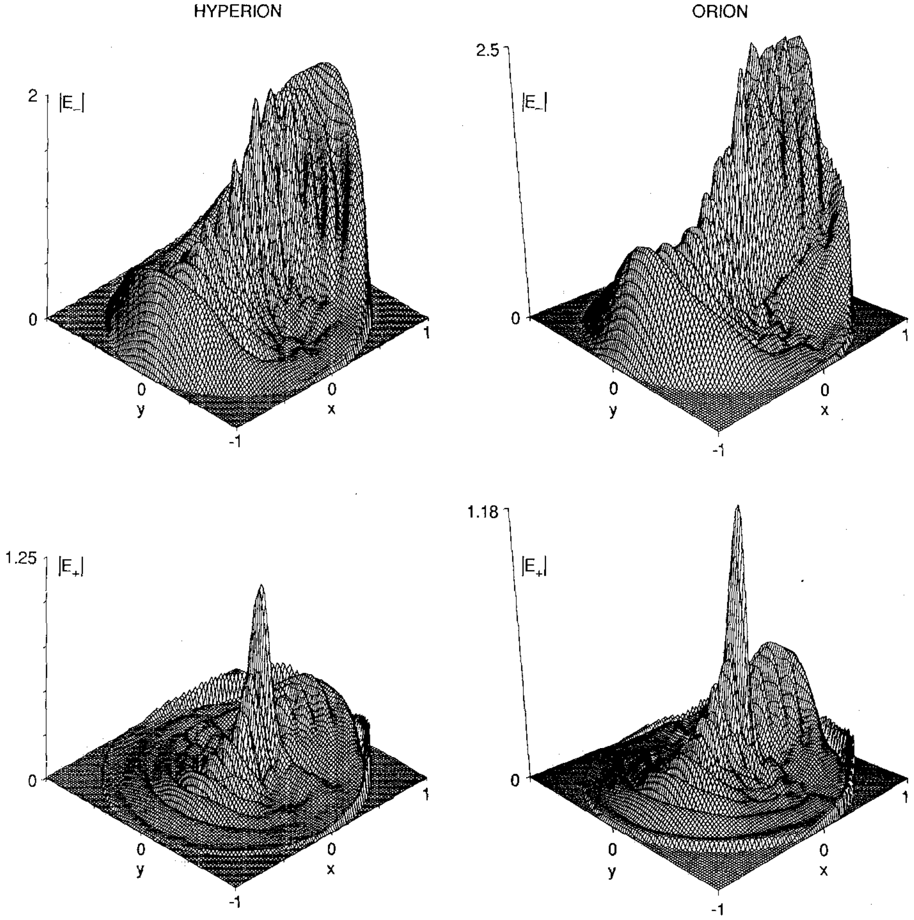

FIG. 2. 3D plots of $|E_+|$ and $|E_-|$ amplitudes for the $n = 22$ toroidal component and the TFTR parameters.

The dependence of the plasma loading resistance on ν/ω is stronger for the low-field antenna than for the high-field antenna. Apparently, the effective collisionality ν allows for some wave absorption at the main cyclotron resonance, which depends strongly on ν/ω. In the case of a low-field antenna, the wave goes through the cyclotron resonance before being absorbed at the two-ion hybrid resonance. However, in the case of high-field launching, the wave is absorbed at the two-ion hybrid resonance before reaching the cyclotron resonance layer.

From the discussion of the block-tridiagonal matrix solver, it is clear that it is [illegible] M). Moreover, the radius is divided into regions in such a way that the grid points can be concentrated in regions requiring higher resolution. In general, radial grids from 60 to 300 points have been used in the calculations discussed here. For high enough densities or when $E_{\|} = 0$, those radial grids have resulted in well-converged solutions. Under these conditions, 80 radial grid points have been used routinely,

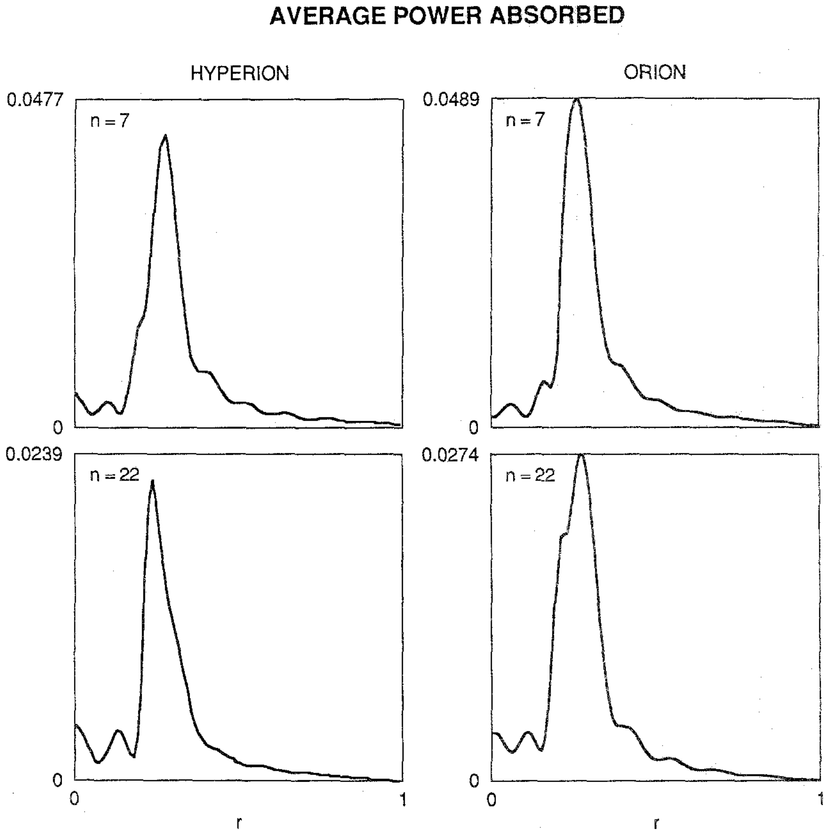

FIG. 3. Flux-surface-average power deposition profiles for $n = 7$ and 22 in W/m^3.

with good results. However, when $E_{\|} \neq 0$ and the density is low enough that the slow wave is not evanescent, finer radial grids are required. The problem of convergence under these conditions is rather more complicated and presently under study, and it wil not be discussed in this paper.

One of the most interesting problems in relation to the convergence of the fast-wave propagation solution refers to the poloidal mode spectrum. The poloidal mode spectrum for the oscillating fields has two main features (Fig. 7), a narrow peak at very low m values, generally at $m = 1$, with a half-width of 3 or 4 m values, and a broad background which can go up to m values of the order of 20 to 40. In comparing the results for toroidal and cylindrical geometry with the same plasma parameters, it is observed that the narrow peak is very similar, but the background has a broader spectral width in toroidal geometry (Fig. 7). Detailed analysis of the results reveals that the width of the central peak is correlated with the poloidal localization of the antenna (Fig. 8), while the background does not seem to be

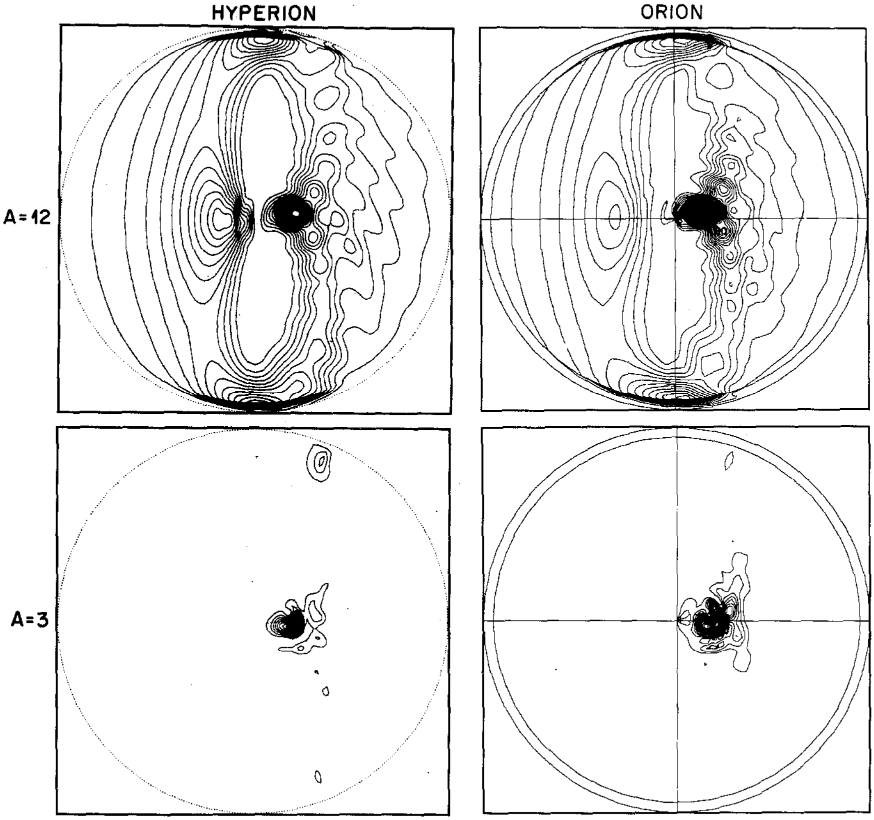

FIG. 4. Local power deposition contours for the TFTR, parameters with an $m = 0$ antenna for axpect ratio $A = 3$ and 12.

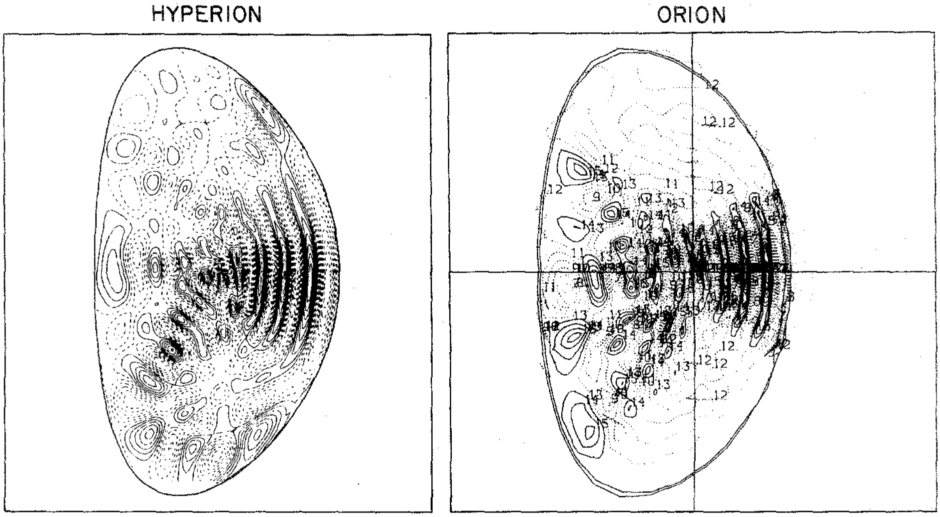

FIG. 5. Contour plots of the Im E_- amplituce for the $n=7$ toroidal component and the TFTR parameters. Here the plasma cross section has been shaped with an ellipticity $\kappa = 1.8$ and triangularity 0.3.

directly affected by it. However, the spectral width of the background is correlated mostly with characteristics of the resonance region, which depend on the value of ν/ω, geometry, and poloidal field strength.

In toroidal geometry, surprisingly few poloidal modes are required to obtain converged values for the plasma loading resistance (Fig. 9). In general, about 10 to 15 modes are required for this case. Figure 9 shows the plasma loading resistance vs the antenna resistance for different values of M. It can be seen that the energy con-

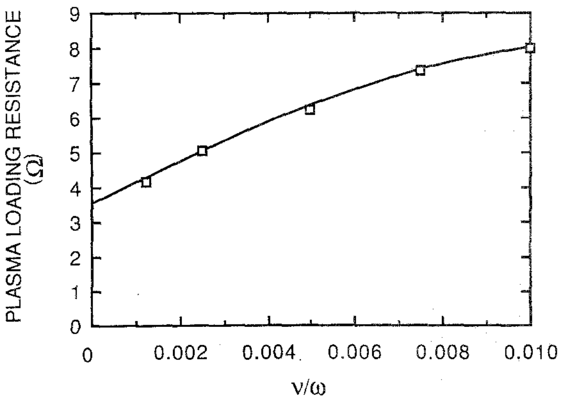

FIG. 6. Dependence of the loading resistance on the ν/ω parameter for $n=7$ toroidal component.

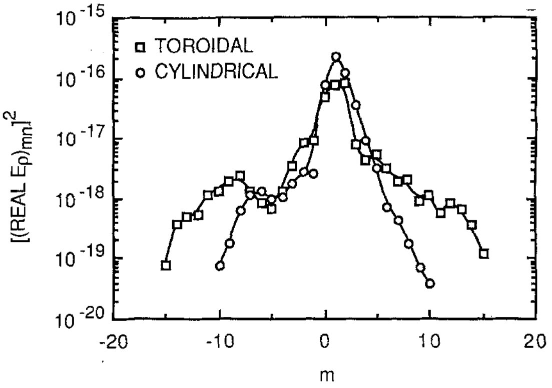

FIG. 7. Poloidal mode spectrum of the real part of the radial electric field component. The parameters are the same as those in Fig. 1, with and without toroidal effects.

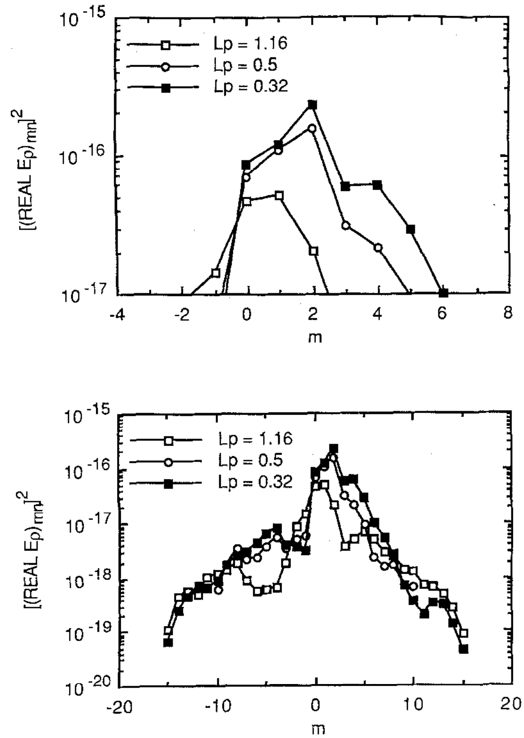

FIG. 8. Poloidal mode spectrum of the real part of the radial electric field component for different values of the poloidal length of the antenna. The top is a blowup of the low-m range of the spectrum at bottom.

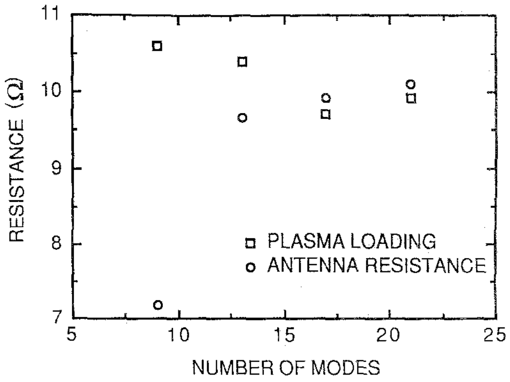

Fig. 9. Comparison of the plasma loading resistance and the antenna resistance, showing the convergence with the number of poloidal mode numbers as well as the increased accuracy of the energy conservation condition.

servation criterion, Eq. (41), gives a good measure of the convergence of the solution. The number of modes required depends on the geometry of the resonance as well as the sharpness of the resonance as influenced by the effective collisionality. In general integrated quantities, such as the radial heating profile or especially the total loading presented here, converge more rapidly than the field structures themselves.

5. Comparison of Toroidal and Cylindrical Geomtery Results

Comparisons of results for toroidal and cylindrical geometry are always subtle because conclusions can depend on how these comparisons are made. Here, the comparisons have been made for the same aspect ratio, q-profile, antenna dimensions in real space, and antenna current. The tokamak parameters for these studies are the same TFTR parameters used in Section 4. Because of the small aspect ratio, $A=3$, it is an interesting case for comparison. Under these conditions, one of the main differences between toroidal and cylindrial geometry is the local value of k_ϕ, the local toroidal wave number. For a fixed n value, $k_\phi = n/R_0$ in cylindrical geometry. Therefore, k_ϕ has a constant value in the whole plasma region. However, in toroidal geometry, $k_\phi = n/R$ and changes substantially from the inside to the outside of the torus.

For the case of low-field antennas, the spatial structure of the oscillating field for a given mode does not change significantly in going from cylindrical to toroidal geometry (Fig. 10). The plasma loading resistance n spectrum is somewhat broader for the toroidal geometry case, with values about 20% higher at low n (Fig. 11). This leads to differences of the order of a factor of two for the total loading

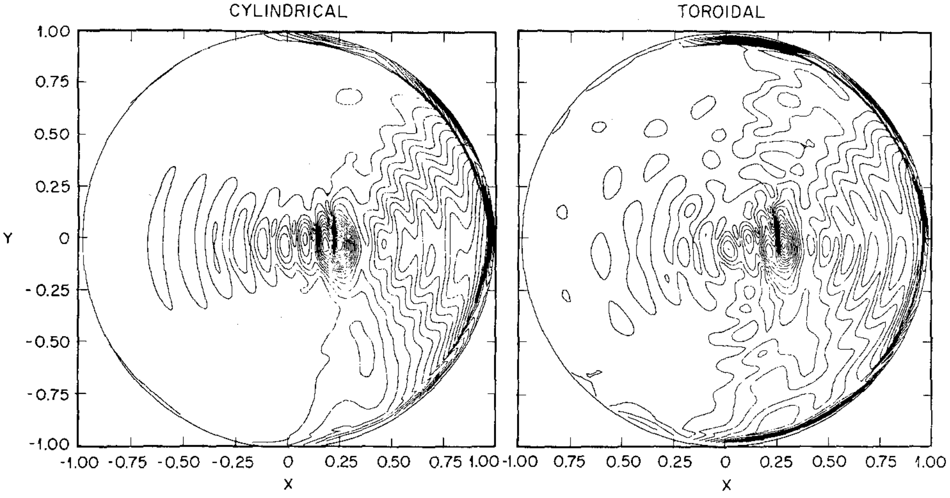

FIG. 10. $|E_+|$ in toroidal and cylindrical geometry for the low-field antenna case ith the $n=7$ toroidal component.

resistance. For a high-field antenna, the discrepancy between cylindrical and toroidal geometry results is more significant (Fig. 12). In this case, the cylindrical geometry results are larger than the toroidal ones; at low n the difference is of the order of 60%, and for the integrated values the difference is a factor of four. Most of the observed differences can be accounted for by the change of k_ϕ. If the local fast-wave dispersion relation is plotted for a fixed n value across the plasma diameter for the cylindrical (Fig. 13a) and toroidal (Fig. 13b) cases, one can see that the diference in local k_ϕ values leads to a smaller evanescent layer at the outside and to a larger one in the inside for the toroidal geometry case. For this parameter regime, in which the wavelength of the fast wave is large than or comparable to the distance between the cutoff and the two-ion hybrid resonance, there

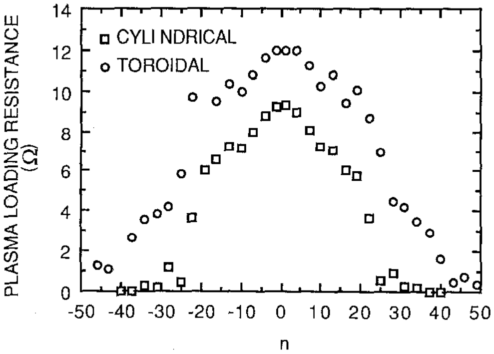

FIG. 11. Plasma loading resistance n-spectrum comparison for the case in Fig. 10.

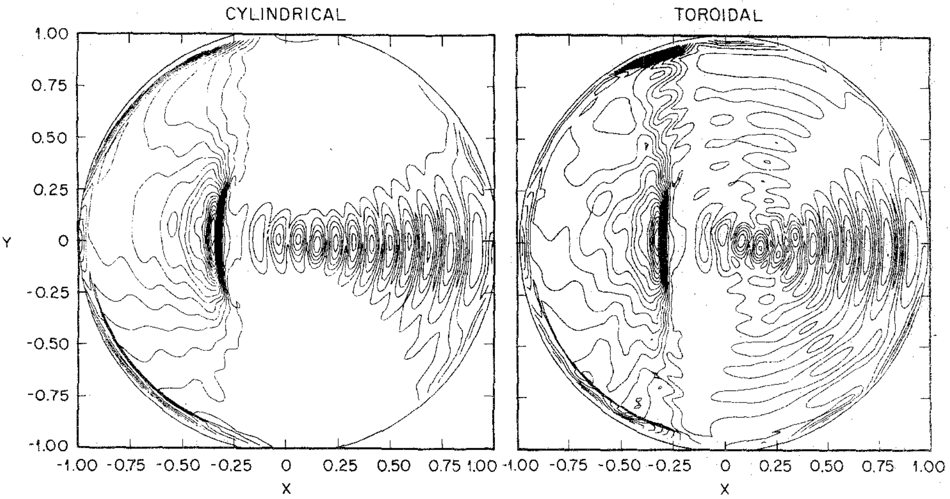

FIG. 12. $|E_+|$ in toroidal and cylindrical geometry for the high-field antenna case with the $n=7$ toroidal component.

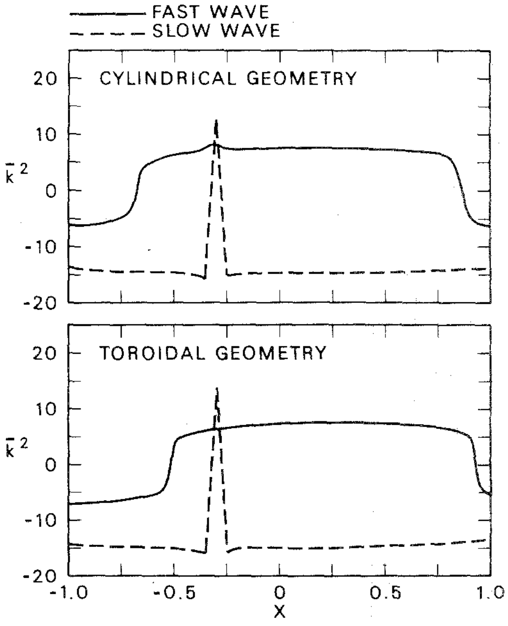

FIG. 13. One-dimensional dispersion relations for the fast and slow wave, plotted for fixed n across the plasma diameter in cylindrical and toroidal geometry. In the linear dispersion relation for the toroidal case, k_z has been replaced by n/R.

is very little reflection at the cutoff. Therefore, the geometry effects discussed here can offset the effect of the cutoff in the case of low-field launching, which can result in higher absorption for low-field launching, as discussed by Villard [14].

6. CONCLUSIONS

Fourier expansion in poloidal and toroidal angels has been shown to be an efficient numerical technique in solving 2D ICRF wave propagation problems. The use of straight-field-line flux coordinates allows one to solve these problems in toroidal geometry and for shaped plasmas. At present, the main limitation of the method is the size of the matrix to be inverted.

Toroidal effects in the ICRF calculations have been shown to be important for a quantitative estimate of the power deposition. Changes of the order of factors of two to five have been found over comparable cylindrical calculations. Also, results in toroidal geometry are more sensitive to the antenna position than in cylindrical geometry.

Future work will involve the incorporation of the plasma Z functions in the dielectric tensor, with special consideration to the accurate representation of the $k_{\parallel}$ wave vector.

ACKNOWLEDGMENT

We gratefully acknowledge useful discussions with Harold Weitzner and P. L. Colestock.

REFERENCES

1. E. F. JAEGER, D. B. BATCHELOR, H. WEITZNER, AND J. H. WHEALTON, *Comput. Phys. Commun.* **40**, 33 (1986).
2. A. FUKUYAMA, K. ITOH, AND S. ITOH, *Comput. Phys. Rep.* **4**, 137 (1986).
3. L. VILLARD, K. APPERT, R. GRUBER, AND J. VACLAVIK, *Comput. Phys. Rep.* **4**, 95 (1986).
4. D. N. SMITHE, P. L. COLESTOCK, R. J. KASHUBA, AND T. KAMMASH, *Nucl. Fusion* **27**, 1319 (1987).
5. M. BRAMBILLA AND T. KRÜCKEN, in *Controlled Fusion and Plasma Physics: Proceedings of the 14th European Conference, Madrid, 22–26 June 1987*, edited by F. Engelmann and J. L. Alvarez Rivas (European Physical Society, 1987), Vol. 11D, Part III, p. 996.
6. D. J. GAMBIER AND A. SAMAIN, *Nucl. Fusion* **25**, 283 (1985); D. EDERY AND H. PICQ, *Comput. Phys. Commun.* **40**, 95 (1986).
7. R. C. GRIMM, J. M. GREENE, AND J. L. JOHNSON, in *Methods in Computational Physics* (Academic Press, New York, 1976), Vol. 16, p. 253.
8. H. R. HICKS, B. A. CARRERAS, J. A. HOLMES, D. K. LEE, AND B. V. WADDELL, *J. Comput. Phys.* **44**, 46 (1981).
9. J. A. HOLMES, Y-K. M. PENG, AND S. J. LYNCH, *J. Comput. Phys.* **36**, 35 (1980).
10. A. C. HINDMARSH, Lawrence Livermore Laboratory Report UCID-30150, 1977 (unpublished).
11. I. S. DUFF, Harwell Report AERE R.11009, 1983 (unpublished).
12. K. ITOH, S. ITOH, AND A. FUKUYAMA, *Nucl. Fusion* **24**, 13 (1984).
13. L. VILLARD, École Polytechnique Fédérale de Lausanne Report LRP 322/87, 1987 (unpublished).
14. E. F. JAEGER, D. B. BATCHELOR, AND H. WEITZNER, *Nucl. Fusion* **28**, 53 (1988).